NANO · MICRO small
www.small-journal.com

Inhibiting HER3 Hyperphosphorylation in HER2-Overexpressing Breast Cancer through Multimodal Therapy with Branched Gold Nanoshells

*Eva Villar-Alvarez, Irene Golán-Cancela, Alberto Pardo, Brenda Velasco, Javier Fernández-Vega, Adriana Cambón, Abeer Al-Modlej, Antonio Topete, Silvia Barbosa, José A. Costoya, and Pablo Taboada**

Treatment failure in breast cancers overexpressing human epidermal growth factor receptor 2 (HER2) is associated mainly to the upregulation of human epidermal growth factor receptor 3 (HER3) oncoprotein linked to chemoresitence. Therefore, to increase patient survival, here a multimodal theranostic nanoplatform targeting both HER2 and HER3 is developed. This consists of doxorubicin-loaded branched gold nanoshells functionalized with the near-infrared (NIR) fluorescent dye indocyanine green, a small interfering RNA (siRNA) against HER3, and the HER2-specific antibody Transtuzumab, able to provide a combined therapeutic outcome (chemo- and photothermal activities, RNA silencing, and immune response). In vitro assays in HER2$^+$/HER3$^+$ SKBR-3 breast cancer cells have shown an effective silencing of HER3 by the released siRNA and an inhibition of HER2 oncoproteins provided by Trastuzumab, along with a decrease of the serine/threonine protein kinase Akt (p-AKT) typically associated with cell survival and proliferation, which helps to overcome doxorubicin chemoresistance. Conversely, adding the NIR light therapy, an increment in p-AKT concentration is observed, although HER2/HER3 inhibitions are maintained for 72 h. Finally, in vivo studies in a tumor-bearing mice model display a significant progressively decrease of the tumor volume after nanoparticle administration and subsequent NIR light irradiation, confirming the potential efficacy of the hybrid nanocarrier.

1. Introduction

In recent years, the involvement of human epidermal growth factor receptor (EGFR) family in cancer has been extensively investigated. This family is composed of four members: human epidermal growth factor receptor 1 (HER1) (also denoted as EGFR), human epidermal growth factor receptor 2 (HER2) (also denoted as HER2/NEU or ERBB2), human epidermal growth factor receptor 3 (HER3), and human epidermal growth factor receptor 4 (HER4). The overexpression of the HER1, HER2, and HER3 receptors, and the amplification of their related genes is directly linked to the aggressive and metastatic nature of many human epithelial-based tumors.[1,2] All these receptors embody an extracellular ligand-binding region that includes four domains (i.e., I/L1, II/CR1, III/L2, and IV/CR2), a transmembrane domain, and an intracellular receptor domain with tyrosine-kinase activity (except for HER3). When a ligand binds to the extracellular

E. Villar-Alvarez, A. Pardo[+], B. Velasco, J. Fernández-Vega, A. Cambón, S. Barbosa, P. Taboada
Grupo de Física de Coloides y Polímeros
Departamento de Física de la Materia Condensada
Universidad de Santiago de Compostela
Instituto de Investigación Sanitaria de Santiago de Compostela IDIS
e Instituto de Materiales (IMATUS)
Santiago de Compostela 15782, Spain
E-mail: pablo.taboada@usc.es

The ORCID identification number(s) for the author(s) of this article can be found under https://doi.org/10.1002/smll.202303934

[+]Present address: 3Bs Research Group, AvePark, Parque de Ciencia e Tecnologia, Universidade do Minho, Zona Industrial da Gandra, Barco-Guimarães, Braga PT 4704-553, Portugal

DOI: 10.1002/smll.202303934

I. Golán-Cancela, J. A. Costoya
Molecular Oncology Laboratory MOL
Departamento de Fisioloxía
Centro Singular de Investigación en Medicina Molecular e Enfermidades Crónicas (CIMUS)
Facultad de Medicina
Universidad de Santiago de Compostela
Instituto de Investigación Sanitaria de Santiago de Compostela IDIS
Santiago de Compostela 15782, Spain

A. Al-Modlej
Department of Physics and Astronomy
College of Science
King Saud University
Riyadh 11451, Saudi Arabia

A. Topete
Laboratorio de Inmunología
Departamento de Fisiología
Centro Universitario de Ciencias de la Salud (CUCS)
Universidad de Guadalajara
Guadalajara 44340, Mexico

region, a receptor–receptor interaction is promoted resulting in dimerization and activating a downstream signaling including phosphoinositide-3-kinase–protein kinase B/Akt (PI3K/AKT) and RAS/mitogen activated protein kinase, involved in cell survival and cell proliferation, respectively (see Figure S1 in the Supporting Information).[3,4] It is also reported that overexpression of HER2 and HER3 receptors in various human cancers (such as breast cancer, ovarian, pancreatic, bladder, lung, and gastric ones) promotes tumor progression by increasing metastatic potential and acting as a major cause of treatment failure.[5–9] HER2 overexpression is correlated with poor prognosis in breast cancers (BCs). In this line, HER2$^+$ BC patients are treated with monoclonal anti-HER2 antibodies such as Trastuzumab (TZ), approved by the US Food and Drug Administration (FDA) in 2006, that targets the extracellular domain of HER2 receptor, avoiding HER2/HER2 dimerization, as well as activating the immune-mediated responses against HER2-overexpressing cells. TZ has demonstrated promising results as the first line therapy by extending HER2$^+$ BC survival.[10,11] Nevertheless, about 15% of TZ-treated patients develop metastasis and nearly 60% of patients bearing HER2$^+$ BC do not respond to treatment.[12] Recently, it was reported that HER2 activity was related to higher levels of programmed cell death protein 1 (PD-1) ligands, which bind PD-1 receptors in immune cells, then suppressing immunological responses and, therefore, evading immune control and leading to drug resistance by the tumor.[13–16] Thus, new therapies are largely required to improve treatment efficacy and life expectancy of patients.[17]

Recent studies have shown that chemoresistance observed in HER2$^+$ breast tumors is directly related to HER3 overexpression (that usually dimerizes with HER1 or HER2), leading to hyperphosphorylation of the cytoplasmic HER3 tail and involving the serine/threonine protein kinase AKT (p-AKT) activation through the PI3K/AKT downstream signaling. The dysregulation of the PI3K/AKT pathway in BC then promotes the recruitment of immunosuppressive cells as well as an overexpression of PD-L1, causing tumor development, immunosuppression, and resistance to HER2-targeted agents such as TZ.[15,18–20] Moreover, activation of HER3 has been shown to result in a strong activation of the PI3K/AKT signaling pathway of HER2/HER3 heterodimers in colon carcinogenesis.[21] Hence, HER3 may support resistance to anti-HER compounds and other antineoplastic drugs by providing an alternative "escape route" in which tumor cells may bypass either HER family and/or downstream PI3K/AKT-signaling-inhibition-based treatments.[22–25] Then, the effective inhibition of HER3 activity is required to overcome drug resistance and enhance therapeutic efficacy (Figure S1b in the Supporting Information).[26,27]

To improve the effectiveness of treatments, TZ has been combined with other anti-HER3 compounds and antibodies, such as the alpha-specific PI3K inhibitor BYL719,[28] anti-PD-L1 inhibitors/antibodies,[18] or the antibody Pertuzumab,[18,29] which blocks HER2/HER3 heterodimerization; however, phosphorylation by HER3 can be hyperactivated by other growth factors; then, this may suggest that antibodies might not be a sufficient therapeutic option to achieve complete tumor regression.[30,31] Consequently, small interfering RNAs (siRNAs) have emerged as alternative for controlling HER3-mediated cellular proliferation and inhibit HER3 through the downregulation of HER3 messenger RNA (mRNA) and associated protein expression and, consequently, the p-AKT levels, in both cells sensitive and insensitive to HER1 and HER2 inhibitors. Previous studies confirm that the treatment of cancer cells with siRNA against HER3 and monoclonal anti-HER1 or anti-HER2 antibodies improve the treatment efficacy by enhancing drug-mediated antitumor effects via inhibition of cell proliferation and induction of apoptosis on HER2-overexpressing BC cells.[4,30–32] Therefore, such dual (or triple combination if a chemotherapeutic drug is included) not only should inhibit HER3 signaling, but also should eliminate tumor drug resistance.

During the past few decades, nanoparticles (NPs) have generated great interest for biomedical applications as drug delivery. At the present time, some NP formulations were approved by regulatory agencies for cancer therapy, for instance, liposomal doxorubicin (DOXIL, MYOCET), docetaxel-loaded micellar formulations (NANOXEL), or albumin-linked paclitaxel (ABRAXANE), limiting toxicity to healthy tissues. However, new issue sand challenges such as the lack of target specificity and developed toxicities appeared in relation to these novel treatments. Multimodality therapy is emerging as an attractive alternative, consisting of the combination of several therapeutic approaches within a single nanocarrier to obtain synergic cytotoxic effects, appears as an advantageous tool to treat tumors. In the last years, a new class of stimuli-responsive NPs (such as carbon-based, calcium-based, magnetic, or metallic NPs) were developed to combine controlled and sustained drug delivery of a bioactive cargo with other specific therapies triggered by external physical stimulations, for example, ionizing radiations for radiotherapy or light for plasmonic photothermal therapy (PPTT) and photodynamic therapy, respectively, resulting in a cytotoxicity improvement compared with the first generation of liposomal or albumin NPs, for example. Furthermore, these new effective multimodal agents can exploit additional properties to act, for example, as contrast agents for diagnostic bioimaging, giving rise to a nanotheranostic platform.[33–35]

Gold nanoparticles (AuNPs) have generated a great interest in cancer therapy because of their unique optical properties including their tunable strong light absorption and scattering in the visible and near-infrared (NIR) wavelength regions of the electromagnetic spectrum related to their localized surface plasmon resonances, biocompatibility, low toxicity, high chemical and physical stability, and versatility of functionalization (by exploiting the ease of conjugation to the gold surface).[36,37] AuNPs are considered suitable platforms for multimodal therapy due to the possibility of combining chemotherapy and PPTT converting the absorbed light into heat.[38,39] Different types of cancers may be treated by PPTT, in particular, those more superficial or accessible via an optical guide surgery.[39–41] Particularly, gold nanoshells (GNs) are unique NPs as they have a core–shell structure which provided the ability to encapsulate and/or attach/conjugate different cargoes in both the core, shell, and/or surface, and which could be released in a controlled manner by external stimuli as light.[41] The light excitation source can be highly tunable in the NIR region by changing either the materials used in the particle structure, the core-to-shell ratio, the particle size, and/or the surface functionalization, for example.[38,42,43] In addition, GNs can act as nanoantennas, enhancing fluorophores' fluorescence when located at certain distance of the particle

surface. For example, the quantum yield of the NIR probe indocyanine green (ICG), an FDA-approved fluorophore for clinical use, was enhanced from 1% to 80% when localized near a GN surface.[38,43] Furthermore, GNs can allow the development of metallic branched shells (branched gold nanoshells, BGNs), thus, increasing the available surface area for bioconjugation and providing additional localized "hot spots" of near-field enhancement on the tip for enhanced biosensing, bioimaging, and/or therapeutic outcomes.[38,41,44,45]

Hence, in the light of these previous works, a novel therapeutic approach is here proposed by means of the combination of: i) the monoclonal antibody TZ to inhibit the dimerization of HER2/HER3 and activation of the immune response;[10,11] ii) a siRNA for the inhibition of HER3 expression and restoration of cell proapoptotic effects;[30,46] iii) the antineoplastic compound doxorubicin (DOXO), usually used in combination with TZ, for chemotherapeutic activity;[47,48] and iv) if desired, an additional PPTT capability upon stimulation of the nanoplatform with suitable NIR light illumination conditions. To combine all the previous therapeutic strategies in a single nanocarrier, BGNs were selected. This hybrid NPs are constituted by a polymeric poly(D,L-lactide-*co*-glycolide) (PLGA) core in which DOXO is encapsulated;[49,50] and an outer porous gold shell providing PPTT capability under suitable light illumination conditions as well as a convenient surface chemistry for siRNA binding through thiol chemistry to get suitable transfection levels into the tumoral cells. In addition, to provide the nanoplatform with suitable colloidal stability in physiologically relevant medium and active HER2 targeting ability, BGN surfaces were functionalized with a layer made of a cross-linked human serum albumin (HSA)–ICG–TZ conjugation complex (HSA–ICG–TZ).[50,51] ICG was selected to monitor the NP biological fate taking advantage of its NIR fluorescence properties, incorporating bioimaging ability to the nanoplatform.[50–53] Hence, the current nanoplatform (coded as DOXO-loaded BGNs@HSA–ICG–TZ/siRNA) should provide an enhanced therapeutic outcome by the HER2 targeting ability using TZ and subsequent inhibition of protein expression with the HER3 knockdown activity through siRNA transfection, being not only an effective therapeutic combination but also enhancing the complementary chemoactivity of DOXO by overcoming potential chemodrug resistance in breast tumors. Consequently, a more efficient multimodal and multipathway therapeutic treatment might be expected.

In vitro cell viability assays confirmed that the DOXO-loaded BGNs@HSA–ICG–TZ/siRNA NPs provide an enhanced cytotoxic activity compared to either BGNs@HSA–ICG–TZ/siRNA or BGNs@HSA–ICG–TZ controls, and demonstrates that the multimodal therapeutic combination of HER2 antibody, siRNA against HER3, and DOXO is highly effective against drug-resistant HER2-overexpressing metastatic breast SKBR-3 cells. Since the present hybrid NPs are NIR-resonant, the simultaneous effect of localized NIR-induced hyperthermia and chemotherapy provided further increases in cell toxicities at rather lower DOXO concentrations under mild NIR illumination conditions. Western blot (WB) analysis highlights HER2, HER3, and p-AKT pathway inhibitions occurring after 24 h of incubation in the absence of NIR illumination. Conversely, under NIR light irradiation, an enhancement of both phosphorylation via p-AKT and HER2 expression is noted, which might suggest that cells activated an alternative route of resistance in the presence of light. In this regard, previous works in photo-biomodulation with NIR light have shown an increment of adenosine triphosphate (ATP) production and cell proliferation through an activation of p-AKT pathway[54] but it is still unknown how light stimulation contributes to such activation.[55] Finally, preliminary in vivo studies point to important accumulations of the hybrid NPs within the tumor areas, with clear evidence of tumor growth inhibition. Some particle accumulation was also noted in liver and spleen as detected by fluorescence optical imaging with no associated toxic effects, as observed from tissue histology.

2. Results and Discussion

2.1. Synthesis and Characterization of Hybrid DOXO-Loaded BGNs@HSA–ICG–TZ/siRNA Nanoplatforms

DOXO-loaded BGNs were obtained as described previously with some modifications (see the Experimental Section for details, and Figure S2 in the Supporting Information).[49,50] The polymeric PLGA cores of BGNs stabilized with a chitosan shell were obtained through a modified nanoprecipitation method, in which the previously hydrophobized chemotherapeutic drug DOXO (see the Experimental Section for details) was incorporated. The positive electrical surface charge of the chitosan layer was further used to attach Au seeds to grow the branched porous multicrystalline gold shell around the polymeric core by means of a seed-mediated reduction reaction (see Figure S3 in the Supporting Information). The size of the resulting hybrid nanoplatform was ≈94 nm in phosphate-buffered saline (PBS) (**Figure 1**a, see also Figure S3 in the Supporting Information) giving rise to a broad NIR plasmon band located in the range from ≈680 to 780 nm (Figure 1b).

The nanoplatform surface was modified with a HSA–ICG–TZ protein complex to achieve sufficient colloidal stability under physiological conditions together with targeting ability to the hybrid nanocarrier.[36,37,50] The complex was formed by incubation of mildly denatured HSA in the presence of the ICG dye followed by bioconjugation of TZ through carbodiimide chemistry (see Figure S4 and Table S1 in the Supporting Information for details). Incubation of the protein complex with the hybrid BGNs led then to the formation of a surface layer surrounding the nanoplatforms (Figure 1b). Next, siRNA was attached through thiol chemistry under suitable conditions by exploiting favorable Au—S and S—S bonds with the gold shell and the HSA protein, respectively.[36,56] The characteristic peak of bound RNA chains at 260 nm in the UV–vis spectra of the nanoplatform is shown in Figure 1b. The hydrodynamic size and surface charge of BGNs@HSA–ICG–TZ/siRNA NPs were ≈117 ± 11 nm and −14.9 ± 5.1 mV, respectively, which confirms the successful attachment of siRNA molecules onto the hybrid particles (see also Table S2 in the Supporting Information). The observed ≈20–25 nm NP size increase after surface functionalization is consistent with the formation of the protein complex layer surrounding the gold outer surface. The enzyme linked immunosorben assay (ELISA) confirmed the incorporation of 3 ± 1 TZ molecules per particle. On the other hand, the amount of siRNA attached to the hybrid nanoplatform was determined to be 5.48 nM of siRNA using a Qubit RNA quantification assay. Meanwhile, DOXO

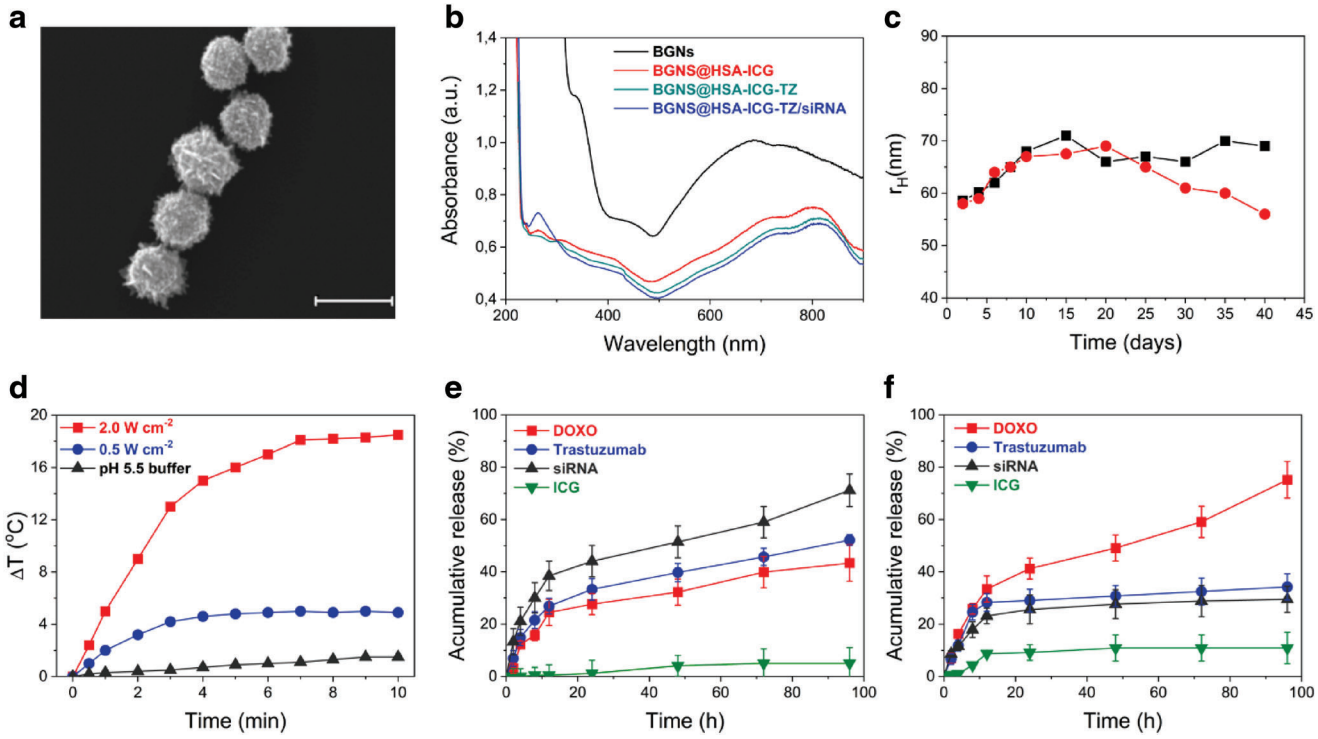

Figure 1. A) Scanning electron microscopy (SEM) images of BGNs; scale bar ≈ 100 nm. B) UV–vis spectra of bare BGNs (black), BGNs@HSA–ICG (red), BGNs@HSA–ICG–TZ (green), and BGNs@HSA–ICG–TZ/siRNA (blue) in PBS at pH 7.4 and room temperature. C) Temporal size evolution of BGNs@HSA–ICG–TZ/siRNA NPs in physiological mimicking media of pH (■) 7.4 and (●) 5.5 containing 10% v/v FBS at 37 °C ($n = 3$). Uncertainties are below 10% (not shown for clarity). D) Temperature increases of BGNs@HSA–ICG–TZ/siRNA nanoplatform in aqueous solution at pH 5.5 with 10% v/v supplemented FBS as a function of time under NIR light irradiation (808 nm) at (■) 2.0 and (●) 0.5 W cm^{-2}. Temperature increases of (▲) pure aqueous solution of pH 5.5 with 10% v/v supplemented FBS under irradiation of 2 W cm^{-2} are also shown for comparison ($n = 3$). Uncertainties are estimated below 8% (not shown). In vitro cumulative release profiles of (■) DOXO, (●) TZ, (▲) siRNA, and (▼) ICG from DOXO-loaded BGNs@HSA–ICG–TZ/siRNA nanoplatforms at pH E) 7.4 and F) 5.5 supplemented with 10% v/v FBS in the absence of NIR light irradiation ($n = 3$). All data were shown as mean ± SD.

encapsulation inside the polymeric core was determined by fluorescence spectroscopy to be 275.0 ± 0.6 nM. Finally, 0.33 ± 1.30 nM of ICG was attached to the hybrid particles as determined by UV–vis and fluorescence measurements. siRNA, DOXO, and ICG were determined at a constant NP concentration of 5×10^9 NPs mL^{-1}.

The hybrid nanoplatforms exhibited good colloidal stability (see the Supporting Information and the Experimental Section for details) upon incubation at 37 °C in culture medium at both pH 7.4 and 5.5 in the presence of 10% v/v fetal bovine serum (FBS) as observed from the negligible changes in NP size with time, which points to the capability of the HSA stealth coating to avoid NP aggregation (Figure 1c).[36,57] Besides the colloidal stabilization effect, the coating layer can also act as a biocompatible and stealth layer which should reduce nonspecific adsorption of plasma proteins and subsequent recognition of the hybrid nanocarrier by the reticuloendothelial system.[36,58]

BGNs@HSA–ICG–TZ/siRNA nanoplatforms also demonstrated an excellent photothermal response. Temperature increments of ≈4 and ≈18 °C were achieved under excitation with a NIR laser irradiation of 808 nm at 0.5 and 2.0 W cm^{-2} for 10 min, respectively. In comparison, only an increase of 1 °C was noted when simply irradiating the control buffer solution at the largest fluency (Figure 1d). Temperature rapidly rises within the first 3–6 min of irradiation leveling off afterward. The present data demonstrated the capability of the hybrid platforms to either inducing cell/tissue ablation (when temperatures are above 43–45 °C), or thermal cell/tissue sensitization (when below 43 °C) depending on the particle concentration and illumination conditions.[59,60]

DOXO, TZ, and siRNA release profiles from DOXO-loaded BGNs@HSA–ICG–TZ/siRNA nanoplatforms were evaluated in aqueous solutions supplemented with 10% v/v FBS at both neutral (pH 7.4) and acidic (pH 5.5) conditions through dialysis experiments in the absence and presence of 808 nm NIR light irradiation (0.5 and 2.0 W cm^{-2}). To quantify the potential influence of the surface desorption of the HSA–ICG complex from the hybrid NPs (if any), release profiles of the ICG–HSA complex at the different solution and illumination conditions tested were also measured. In vitro cumulative releases of DOXO, ICG, TZ, and siRNA show a 12 h burst phase followed by a more sustained release pattern at the different solution conditions (Figure 1e,f) in the absence of NIR illumination. At pH 7.4, 25% and 36% DOXO are released from DOXO-loaded BGNs@HSA–ICG–TZ/siRNA nanoplatforms after 12 and 72 h incubation, respectively (Figure 1e). Conversely, under acidic conditions, ≈33% of the initially loaded DOXO is released at 12 h and 58% after 72 h, respectively (Figure 1f). This faster release is originated

from both the larger hydrolytic degradation rate of PLGA and the protonation of DOXO amine groups, which involves an enhancement of drug hydrophilicity and subsequent decrease in affinity for the hydrophobic polymeric matrix, thus, favoring its diffusion out of the particle core. Conversely, for both TZ and siRNA, a different behavior is observed. For TZ, ≈45% is released at pH 7.4 compared to 32% at pH 5.5 after 96 h of incubation (Figure 1e,f) probably due to certain amide bond degradation.[61,62] Protein is hardly desorbed as confirmed by the low amount of released ICG dye.[36,37,50,51,63] In the case of siRNA, ≈70% is released at pH 7.4 compared to 28% at pH 5.5 after 96 h pointing to the influence of solution pH on the physical interactions between siRNA molecules and the particle coating layer as well as on Au—S bond stability.[56]

In the presence of NIR illumination (0.5 or 2.0 W cm^{-2} for 3 min), DOXO, TZ, and siRNA release is clearly enhanced. An increment of DOXO release from ≈73% to ≈86% and 92% at 0.5 and 2.0 W cm^{-2} after 96 h of incubation was noted, respectively (Figure S5a, Supporting Information), consequence of the faster drug diffusion through the polymeric matrix after its progressive softening as the irradiation fluency increases. In a similar way, an enhancement in TZ and siRNA releases upon NIR light illumination was also observed from ≈34% to ≈59% and 65% (Figure S5b, Supporting Information), and from ≈31% to 48% and 55% after 96 h of incubation at 0.5 and 2.0 W cm^{-2}, respectively (Figure S5c, Supporting Information). In this regard, the potential increment of reactive oxygen species (ROS) released by ICG molecules[64] (approximately proportional to the power density) might additionally contribute to amide bonding hydrolysis in the case of TZ,[62] whereas the temperature increments might disturb the interactions between siRNA and the protein coating favoring, then, the release.[56,65–67]

An evaluation of the potential cytotoxicity and therapeutic effect of the nanoplatforms was carried out increasing the degree of complexity using, in the corresponding cases, a biologically inactive siRNA (coded as scrambled siRNA, siRNAsc): BGNs@HSA–ICG, BGNs@HSA–ICG/siRNAsc, BGNs@HSA–ICG–TZ/siRNAsc, BGNs@HSA–ICG–TZ/siRNA, and DOXO-loaded BGNs@HSA–ICG–TZ/siRNA NPs. A cytotoxic concentration-dependent behavior within the concentration range from 1×10^9 to 1×10^{12} NP mL^{-1} after 24 and 48 h of incubation in metastatic SKBR-3 BC cells was noted for BGNs@HSA–ICG and BGNs@HSA–ICG/siRNAsc NPs (**Figure 2**a,b), with viabilities above 70% at concentrations below 1.0×10^{10} NP mL^{-1} as well as no observation of alterations in protein expression levels (Figure 2c,d, see also the Supporting Information for additional details and Figures S6 and S7 in the Supporting Information for the original raw WB images). In addition, the inclusion of TZ in the hybrid NPs (BGNs@HSA–ICG–TZ/siRNAsc) resulted in a temporal HER2 downexpression leading to a transient decrease in cell proliferation after 24 h of incubation (see Figure 2a,e, and also Figure S8 in the Supporting Information for the original raw WB image).[68] TZ administered as a single therapeutic agent cannot preclude the phosphorylation associated to heterodimer formation which reactivates the p-AKT pathway and subsequent cell proliferation, and explains the detection of HER3, p-AKT proteins, and the restoration of HER2 expression in WB data after 48 h of incubation.[27,69]

Conversely, when a siRNA to inhibit HER3 expression is coincorporated in the nanoplatform (BGNs@HSA–ICG–TZ/siRNA) (see Figure S10a in the Supporting Information for further details), a significant inhibition of HER2, HER3, and p-AKT levels is clearly observed (Figure 2f and Figure S10a in the Supporting Information for the original raw WB image). In particular, an important HER2 and HER3 knockdown effect at 24 h of incubation is observed, which correlated with the reduction in p-AKT signaling,[27,68–70] and agrees with the larger cell toxicities observed after 48 h (Figure 2h). Nevertheless, after this incubation time, a progressive restoration of protein expression levels is also noted (Figure 2f), which might allow the proliferation of the still alive cells at longer times if no further nanoplatform administration is made.

The incorporation of DOXO in the nanoplatform involves an enhancement of cell mortality from ≈35% to ≈55% after 48 h of incubation (Figure 2h), thanks to the combined therapeutic effect of both TZ and the siRNA against HER3 which effectively decreases HER2 and HER3 expressions (see **Figure 3**b below), thus, facilitating the chemical bioactivity of DOXO. In fact, the free DOXO concentration used (5.54 μM, equivalent to the drug-loaded concentration in 1×10^{11} NPs mL^{-1}) did not induce relevant toxicity to cells (Figure 2g) but a small enhancement in cell proliferation was noted due to the multidrug resistant character of the tested cell line as consequence of HER2/HER3 heterodimerization and/or HER2 homodimerization (Figure 2h).[27,69,71] It is also worth mentioning that cell cytotoxicity in the time frame analyzed is not enhanced since DOXO releases through the NP porous shell by simple diffusion, and this process requires relatively long times to achieve a therapeutical optimal drug concentration inside cells (see Figure 1e,f).

On the other hand, cells treated with free DOXO, BGNs@HSA–ICG–TZ/siRNA, and DOXO-loaded BGNs@HSA–ICG–TZ/siRNA particles at a concentration of 5.0×10^9 NP mL^{-1} were also subjected to 808 nm NIR light irradiation with a continuous wave diode laser at fluencies of 0.5 and 2.0 W cm^{-2} for 3 min to observe the influence of NIR laser irradiation on the therapeutic efficacy. As shown in Figure 3a, NIR light was nontoxic to control cells but cell cytotoxicity is relatively enhanced after nanoplatform uptake by cells in a time- and fluency-dependent manner. DOXO-loaded BGNs@HSA–ICG–TZ/siRNA NPs show a relatively larger toxic effect than BGNs@HSA–ICG–TZ/siRNA ones attributable to the chemoactivity of DOXO, effect particularly relevant at the highest fluency used (71% and 88% of cell mortality at 2.0 W cm^{-2} after 48 and 72 h of incubation, respectively). Hence, NIR light and the subsequent temperature increase may also help to enhance drug diffusion through the polymeric matrix, thus, favoring the chemotherapeutic action of the nanoplatform.[35,49,50]

Cytotoxicity data were additionally supported by WB analysis (Figure 3b; see Figure S9 in the Supporting Information for the original raw WB images). After the administration of BGNs@HSA–ICG–TZ/siRNA NPs to cells in the absence of NIR light irradiation, HER2, HER3, and p-AKT protein expressions were inhibited after 24 h of incubation; conversely, cell signaling was progressively restored at longer incubation times. When DOXO is coadministered within the particles, the inhibition of the protein levels at 24 h is abruptly reduced. It has been previously reported that activation of

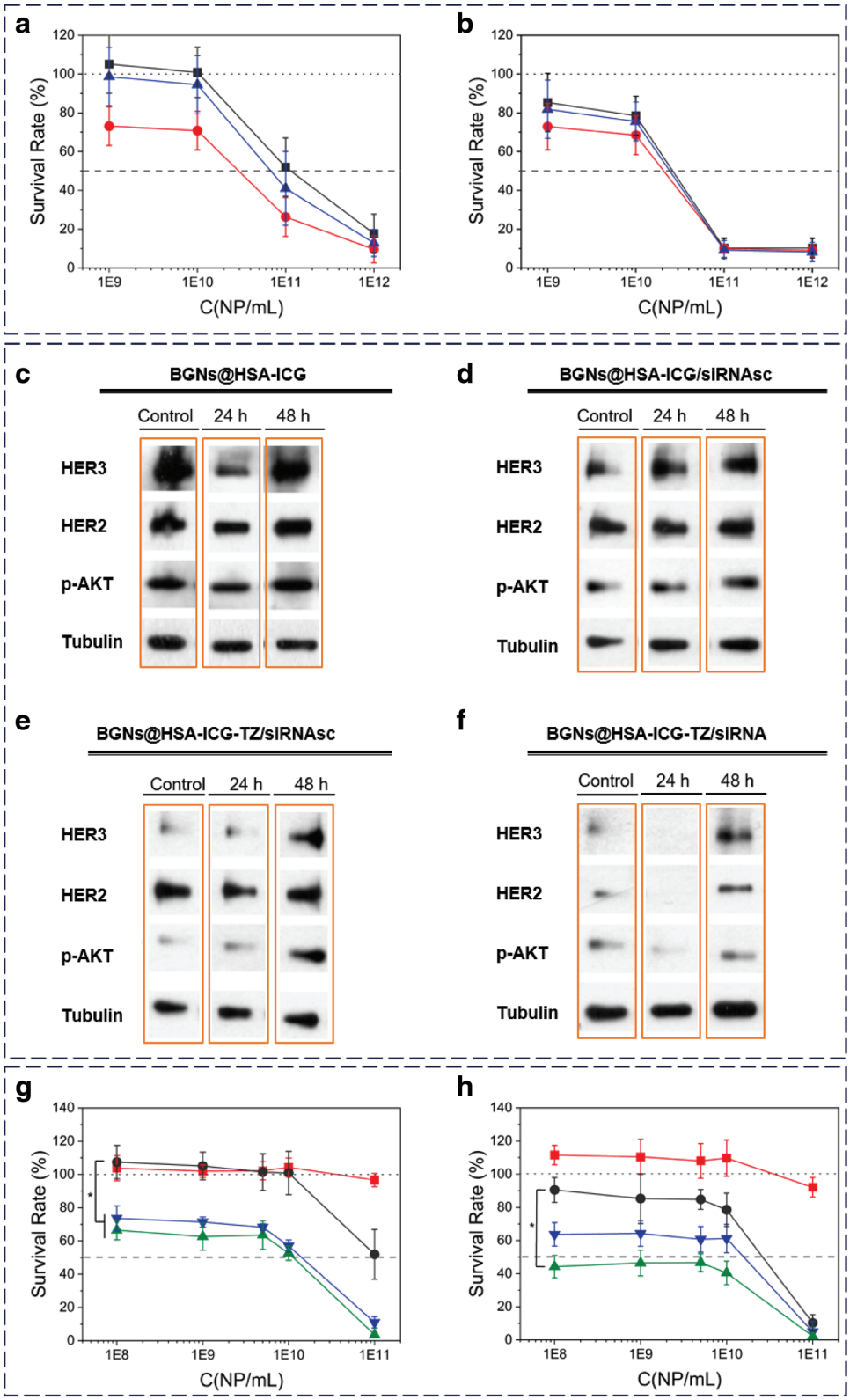

Figure 2. Influence of particle concentration on cell viability for bare BGNs@HSA–ICG (■), BGNs@HSA–ICG/siRNAsc (▲), and BGNs@HSA–ICG–TZ/siRNAsc (●) in breast SKBR-3 cancer cells after A) 24 and B) 48 h of incubation. Dashed (50%) and dotted (100%) lines are only to guide the eye ($n = 3$). Western blot analysis for HER3, HER2, p-AKT (Ser473), and tubulin (as a loading control) protein expressions from SKBR-3 breast cancer cells after administration of C) BGNs@HSA–ICG, D) BGNs@HSA–ICG/siRNAsc, E) BGNs@HSA–ICG–TZ/siRNAsc, and F) BGNs@HSA–ICG–TZ/siRNA NPs (at 5.0×10^9 NP mL^{-1}) after 24 and 48 h of incubation ($n = 3$). Control here denotes cells without particles after 24 h of incubation. Control

p-AKT through the HER2/HER3/p-AKT signaling pathway after DOXO treatment leads to resistance to chemotherapy.[27,71] Specifically, it was reported that SKBR-3 cells show a high proliferative activity after DOXO treatment, as observed for other HER2-overexpressing cell lines, which is confirmed by an important increment in the level of p-AKT expression after only 24 h of drug administration.[71] Nevertheless, it is observed that when TZ is attached to DOXO-loaded NPs, a decrease in protein expression of DOXO-induced p-AKT phosphorylation occurs which, in turn, downregulates HER2 and HER3 protein levels over time (Figure 3b).[27] Hence, the combined downregulation of HER2 and HER3 by both the antibody and the siRNA might inhibit HER2/HER3 heterodimer formation, preventing the decrease in p-AKT levels after DOXO treatment and providing the chemotherapeutic agent the capability to overcome cell drug resistance while activating cell apoptosis,[27] in agreement with the observed cell toxicities (Figures 2g,h and 3a).

Conversely, under NIR light irradiation at 0.5 and 2.0 W cm^{-2}, a certain different picture is depicted, that is, an increment in p-AKT expression and in HER2 and HER3 ones are observed after the administration of BGNs@HSA–ICG–TZ/siRNA NPs at 24 h of incubation, being proportional to the NIR power density. This suggests that p-AKT phosphorylation does not stem from HER2/HER2 and HER2/HER3 dimerization. Zhang et al. suggested that the p-AKT pathway can be activated by NIR-laser light,[55] giving rise to an enhancement of ATP production, cell proliferation, and DNA/RNA synthesis.[72,73] Similarly, Li et al. showed that treatment with ionizing radiation induced a similar enhancement of p-AKT protein expression.[27] In addition, activation of p-AKT might arise from ROS-induced generation[64] by ICG dye under the selected illumination conditions as previously demonstrated,[35,49,50] but further experiments would be required to confirm such hypothesis. When DOXO is encapsulated inside the nanoplatform (DOXO-loaded BGNs@HSA–ICG–TZ/siRNA NPs), data show a highly proliferative activity via both DOXO- and light-induced phosphorylation of p-AKT, increasing p-AKT level expression at least after 72 h of incubation and reducing, in consequence, the inhibition of HER2 and HER3 protein levels in comparison to BGNs@HSA–ICG–TZ/siRNA NPs after 24 h. However, at the longest incubation times, HER2 and HER3 protein expression is decreased abruptly; as a result, cell toxicity increases through the synergistic combination of the antibody and the siRNA, the therapeutic action of DOXO, and the photothermal treatment provided by the BGN carrier to overcome potential cell drug resistance.

2.2. In Vivo Biodistribution of the Hybrid Nanoplatforms

The in vivo biodistribution of the bare nanoplatforms, BGNs@HSA–ICG–TZ NPs, was analyzed after intravenously administering 10 mg kg^{-1} of the hybrid particles in NMRI-Fox1nu/Fox1nu nude mice bearing a breast xenograft tumor. ICG was used as the tracking molecule to monitor the NP distribution. In vivo NIR fluorescence optical images revealed the distribution of the nanoplatform, with a fair accumulation in the tumor area (**Figure 4**a). In addition, some signals from liver and brain can be observed. This is certainly striking for the latter organ provided that the blood brain barrier (BBB) should preclude any particle to penetrate into, so that the fluorescence signal might be stem, at least in part, from some ICG–HSA complex desorption from the hybrid NPs, providing enhanced ICG photostability (by avoiding leakage and photobleaching).[51] Transmission electron microscopy (TEM) images also confirmed the presence of the hybrid nanoplatforms within the tumor (Figure 4b), spleen (Figure 4c), and liver (Figure 4d) which are predominant as also observed from fluorescence tomography (Figure 4e); in addition, some presence in the brain can be also noted (Figure S11a, Supporting Information). Furthermore, scarce whole and fragments of NPs were also observed in lungs and kidneys (Figure S11b,c, Supporting Information). NP accumulation in the brain region suggests that the fluorescence signal after 48 h postinjection could be ascribed as a combination of desorbed complexed ICG and hybrid NPs crossing the BBB. Similar were also reported in previous works,[50] supporting this hypothesis. However, additional and more detailed experiments are required to corroborate this hypothesis, which would open up the possibility of using this type of hybrid NPs as specific theranostic nanodevices for the treatment of brain pathologies. In this regard, some previous studies have shown that NP surface coating is a key factor to overcome the BBB for successful brain delivery and/or diagnostics.

2.3. In Vivo Therapeutic Activity of the Hybrid Nanoplatforms

The therapeutic potential of DOXO-loaded BGNs@HSA–ICG–TZ/siRNA NPs was analyzed by intratumorally injecting 10 mg kg^{-1} of the hybrid NPs in the absence and presence of NIR light irradiation (808 nm, at 0.5 and 2.0 W cm^{-2} for 5 min after 6 and 24 h of injection).[39,74–77] Subcutaneous and intratumorally injections of PBS were used as controls. First, it was observed that after injection, the nanoplatforms were clearly accumulated in the tumor, with no signs of migration to other parts of the body even in the presence of irradiation (**Figure 5**a).[53] In addition, tissues were harvested and tumor pathology was assessed in formalin-fixed paraffin-embedded samples by hematoxylin and eosin (H&E) staining. Cell proliferation and apoptosis in the tumor and liver tissues were evidenced by phospho-histone H3 and activated caspase-3 immunostaining, respectively. Untreated tumors showed higher phospho-histone H3 staining than treated ones (Figure 5b), a finding that suggests a reduced proliferation rate after NP administration. In this regard, no histopathological changes such as the disruption of the tissue architecture and loss of cell cohesion were noted upon administration of BGNs@HSA–ICG NPs as a control (not shown). Additionally, caspase-3 activity increased in NP-treated and irradiated tumors, which may reflect the reduced tumorigenic potential of these

at 48 h is not shown for simplicity since data exhibit the fully protein expression recovery clearly. Cell viability of SKBR-3 cells after administration of BGNs@HSA–ICG–TZ/siRNA (▼), DOXO-loaded BGNs@HSA–ICG–TZ/siRNA (▲), BGNs@HSA–ICG (●) NPs, and free DOXO (■) after G) 24 and H) 48 h of incubation. Dotted (100%) and dashed (50%) lines are only to guide the eye ($n = 3$). All the data were shown as mean ± SD. Statistical analysis was performed via a two-tail Student's *t*-test. *$p < 0.05$; **$p < 0.01$; otherwise, $p > 0.05$.

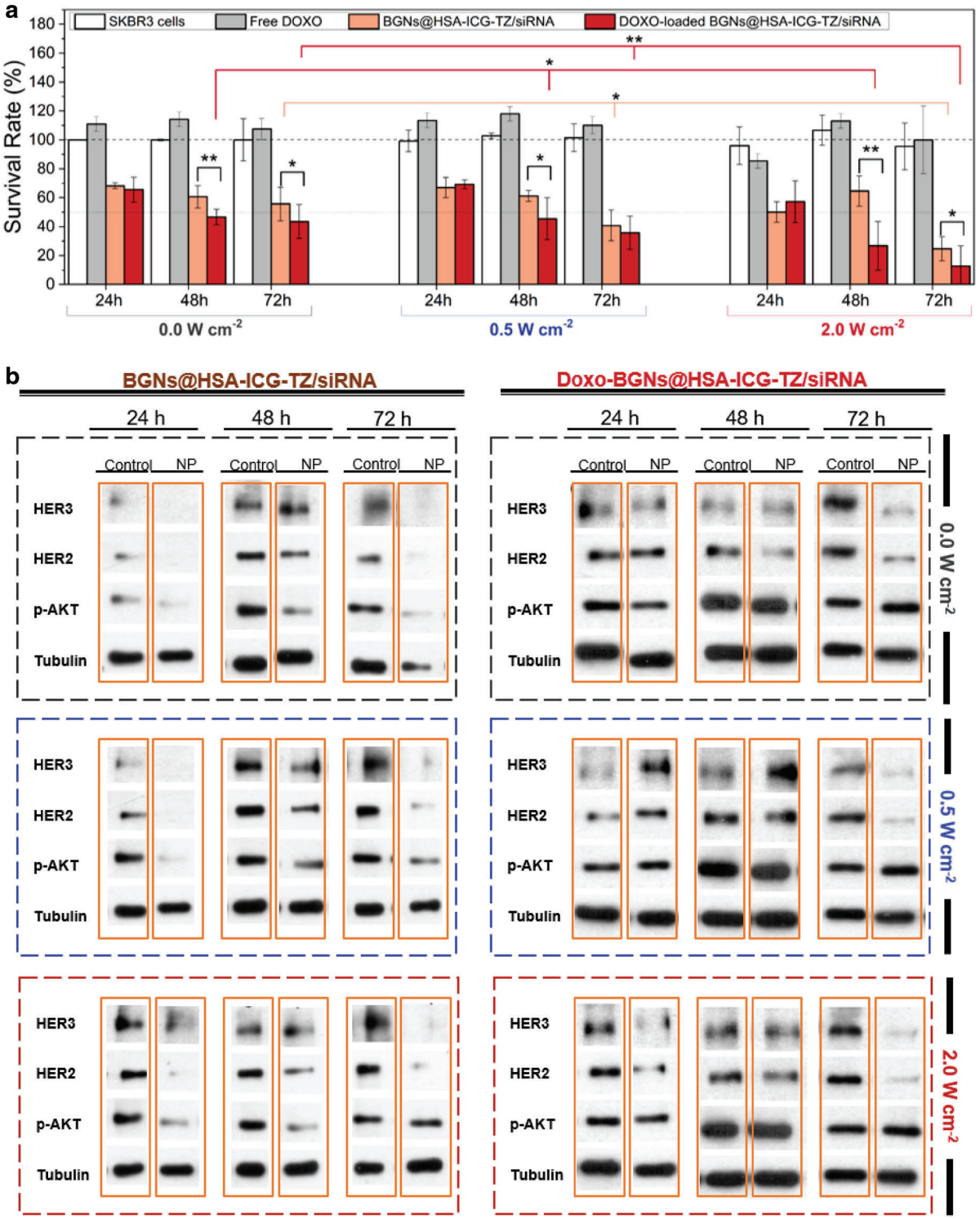

Figure 3. A) Survival rates of SKBR-3 cells exposed to free DOXO (gray), BGNs@HSA–ICG–TZ/siRNA (orange), and DOXO-loaded BGNs@HSA–ICG–TZ/siRNA (red) in the absence and presence of NIR light illumination supplied by a CW laser at 808 nm after 24, 48, and 72 h of incubation at power densities of 0.0, 0.5, and 2.0 W cm^{-2}. Non-treated cells (white) were used as a negative control ($n = 3$). Dotted (50%) and dashed (100%) lines are only to guide the eye. B) Western blot analysis for HER3, HER2, p-AKT (Ser473), and tubulin (as a loading control) protein expression from SKBR-3 BC cells after administration of BGNs@HSA–ICG–TZ/siRNA and DOXO-loaded BGNs@HSA–ICG–TZ/siRNA NPs under NIR light illumination with an 808 nm CW diode laser at fluencies of 0.0 (non-irradiation), 0.5, and 2.0 W cm^{-2} after 24, 48, and 72 h of incubation. The particle concentration was fixed at 5.0×10^9 NP mL^{-1}. Untreated cells were used as a negative control. For each irradiation treatment, a different control was done. All the data were shown as mean ± SD. Statistical analysis was performed via a two-tail Student's *t*-test. $^*p < 0.05$; $^{**}p < 0.01$; otherwise, $p > 0.05$.

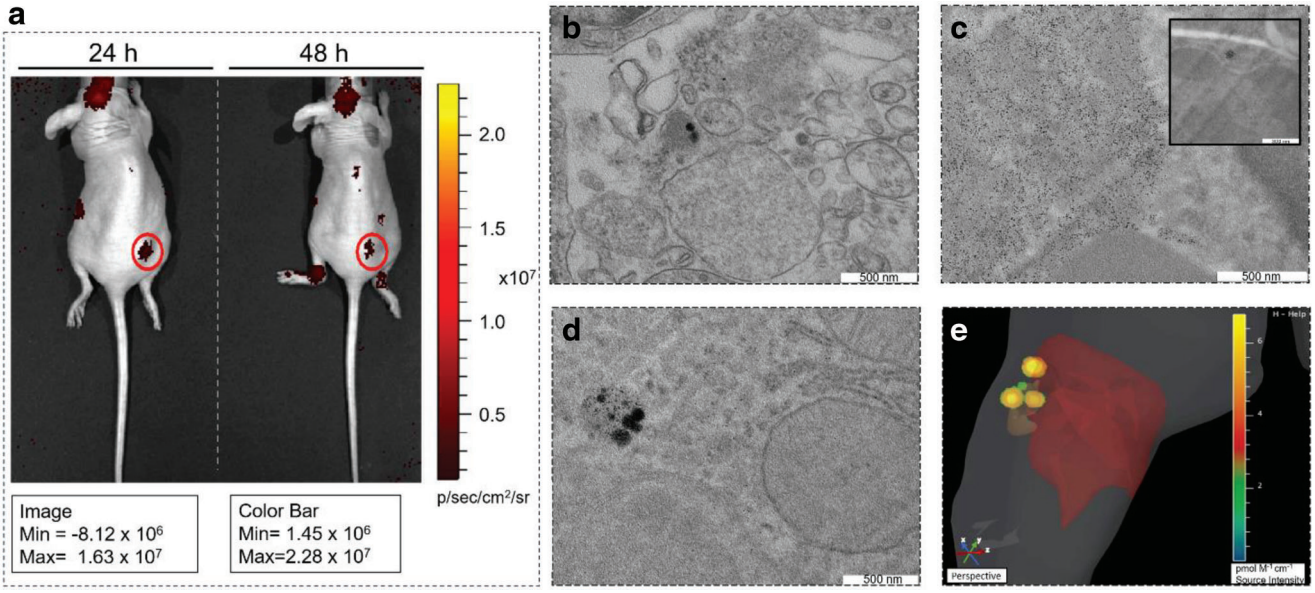

Figure 4. A) In vivo NIR images of breast adenocarcinoma tumor-bearing mice after intravenous tail injection of BGNs@HSA–ICG–TZ NPs. The fluorescence from ICG ($\lambda_{ex}/\lambda_{em}$ = 740/840 nm) was monitored at 24 and 48 h postinjection (n = 3). Tumor area in epifluorescence images is circled in red. TEM images of sectioned tissues of different organs: B) tumor, C) spleen, D) liver harvested after 96 h upon injection; scale bar = 500 nm. The presence of particles or fragments of particles as black dotted points in tissues is clearly observed. E) A 3D fluorescence tomography image denotes the particle accumulation mainly in liver and spleen. Inset in (C) points to some particle degradation/fragmentation in smaller units; scale bar = 300 nm.

cells. There were also no observable changes in tissue structure or enhancement of activated caspase-3 immunostaining in the liver, consistent with the absence of toxicity (Figure 5b).[78]

Furthermore, preliminary evaluation of the tumor size over the time was done after single-dose administration of DOXO-loaded BGNs@HSA–ICG–TZ/siRNA NPs injected intratumorally (10 mg kg^{-1}). Three scenarios were evaluated: absence of irradiation (0.0 W cm^{-2}), and in the presence of light irradiation (808 nm) at low (0.5 W cm^{-2}) and moderate–high fluency (2.0 W cm^{-2}) for 5 min after 6 and 24 h of injection. Intratumoral injections of PBS without any irradiation were used as control (**Figure 6**). An initial tumor size increase was observed during the first 6 days after the nanoplatform administration. Thereafter, different situations were observed: in the absence of irradiation, tumor growth stopped for up to additional 6 days, but then, restarted again. This can be a consequence of the initial therapeutic effect of the nanoplatform provided by the combination of the antibody, the chemodrug, and siRNA; however, the restoration of HER2 and HER3 expressions, as observed from WB data, would lead to the proliferation of new cancerous cells and subsequent tumor regrowth. Conversely, when NIR irradiation is applied, an important tumor size reduction was observed after the initial tumor growth until the mice were sacrificed. This effect is particularly more evident at the highest fluency used (2.0 W cm^{-2}), for which the tumor is completely reduced in two weeks. This would point to the positive effect of NIR light illumination in combination with the chemical activity of the drug; at this respect, light irradiation not only exerts a therapeutic effect but also should stimulate DOXO release favoring the achievement of suitable therapeutic concentrations in the tumor medium which overlay the knockdown of HER protein expression provided by siRNA and TZ biological activities.

3. Conclusion

The overexpressions of HER2 and HER3 oncogenes are involved in the development and progression of certain aggressive types of breast cancer. HER3 confers an additional drug resistance mechanism to the therapeutic action of antineoplastic drugs. To overcome such issues, a multifunctional biocompatible theranostic nanoplatform was designed. This consists of a biodegradable PLGA polymeric core encapsulating the anticancer drug DOXO with a metal shell surface, which is functionalized with the NIR ICG dye, a siRNA for HER3 oncogenic protein knockdown, and the antibody Trastuzumab to selectively binding HER2 receptors and subsequent avoidance of protein dimerization, respectively. It was shown that BGNs@HSA–ICG–TZ/siRNA nanoplatforms display a good colloidal stability upon extensive incubation under physiological-mimicking conditions. Besides, the hybrid NPs exhibit interesting photothermal properties under NIR light illumination giving rise to both solution temperature increments of up to ≈18 °C in less than 5 min and to a NIR-light-triggered and stepwise controlled release behavior of the therapeutic drug cargo.

Cell viability and Western blot analyses revealed that the hybrid nanoplatforms are nontoxic to cells. The combination of Trastuzumab and specific siRNA is able to suppress HER2 and HER3 protein expressions and p-AKT signaling after 24 h of incubation, and which are restored at longer incubation times. When NIR light irradiation is applied, a slight NIR-induced p-AKT phosphorylation correlated with an enhanced kinase activity and cell proliferation is noted. In particular, DOXO-loaded BGNs@HSA–ICG–TZ/siRNA particles display cell survival rates of ≈40–45%, which are further reduced under NIR illumination to only ≈10%. Western blots show an activation of p-AKT expression when DOXO is included and released from the

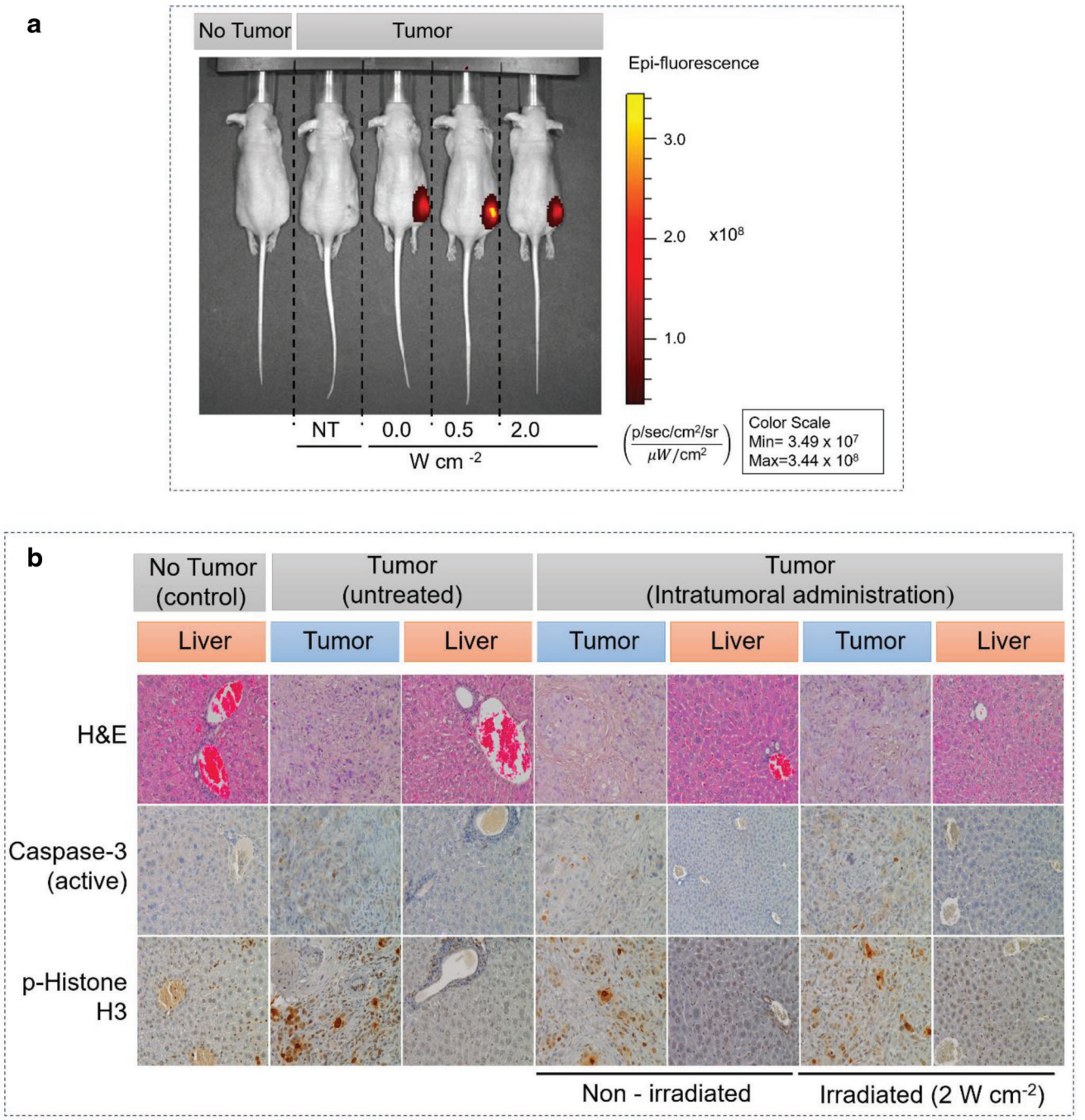

Figure 5. A) NIR images of tumor-bearing mice after subcutaneous injection of breast tumor cells after 6 and 24 h of administration of (from left to right): no tumor and intradermal PBS, intratumoral PBS, and intratumoral DOXO-loaded BGNs@HSA–ICG–TZ/siRNA NPs in the absence and presence of light irradiation (808 nm) at 0.5 and 2.0 W cm^{-2}, respectively (n=3); B) H&E staining, and cleaved caspase-3 and phospho-histone H3 immunostaining of liver and tumor tissues after two weeks for (from left to right): healthy liver tissue, untreated tumor and liver, and DOXO-loaded BGNs@HSA–ICG–TZ/siRNA NPs, and DOXO-loaded BGNs@HSA–ICG–TZ/siRNA NPs administered to tumor under 808 nm light irradiation at 2.0 W cm^{-2}.

nanoplatform as a consequence of drug resistances developed in this kind of cancer cells at short incubation times (24 h). Once HER3 oncogene is silenced at long incubation times (72 h), DOXO can exert its chemotherapeutic activity and induce cell apoptosis.

The preliminary in vivo biodistribution analysis of BGNs@HSA–ICG–TZ nanoplatforms shows an effective and relatively fast NP accumulation in the tumor area, which is maintained even at relatively long times. The present hybrid NPs were mainly eliminated through the reticuloendothelial

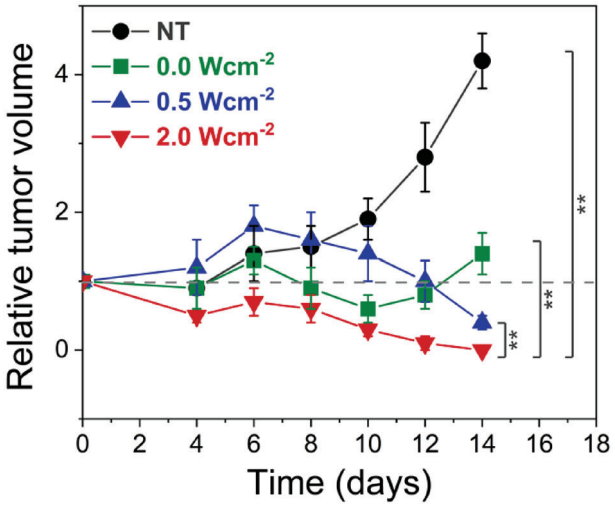

Figure 6. Evolution of the tumor size over time after NP administration: untreated tumor (●); treatment with DOXO-loaded BGNs@HSA–ICG–TZ/siRNA NPs administered to tumor (10 mg kg^{-1}) in the absence (■), and the presence of light irradiation (808 nm) at 0.5 W cm^{-2} (p) and 2.0 W cm^{-2} (▼). Data were presented as mean ± SD. Statistical analysis was performed via the two-tail Student's *t*-test $*p < 0.05$; $**p < 0.01$; otherwise, $p > 0.05$.

system showing no cell damage in liver, as demonstrated by immunostaining and histological analysis. In addition, the hybrid DOXO-loaded BGNs@HSA–ICG–TZ/siRNA nanoplatform was shown to be highly effective in stopping tumor growth and reducing tumor size, in particular, under NIR light irradiation without major affectation to healthy tissues. In this regard, only some apoptotic cells and inflammatory response were found in the tumor area probably as a consequence of the important NP accumulation after intratumoral injection. Furthermore, in spite of this study was focused for $HER2^+$ breast cancer, it opens a door to use this multimodal hybrid nanoplatform for the treatment of other HER2/HER3-overexpressing cancers, as ovarian, lung, colorectum, and head and neck tumors. However, potential subtle modifications and additional studies should be done to confirm the expected therapeutic outcomes of this hybrid nanosystem to treat other types of $HER2^+$ tumors.

4. Experimental Section

Materials: HSA, ICG, PLGA of 38–54 kDa with 50:50 lactide–glycolide ratio, Pluronic F127, hydrogen tetrachloroaureate(III) trihydrate ($HAuCl_4 \cdot 3H_2O$), *N*-(3-dimethylamniopropyl)-3-ethylcarbodiimide hydrochloride (EDC), sulfo-*N*-hydroxysuccinimide (sulfo-NHS), low molecular weight (LMW) chitosan (MW = 111 kDa), potassium carbonate anhydrous, sodium borohydride, sodium azide, sodium citrate tribasic, ascorbic acid, and glutaraldehyde were purchased from Sigma-Aldrich (USA). siRNA against HER3 3′-thio-C3(SS) with target sequence: 5′-ACCACGGTATCTGGTCATAAA-3′; sense strand: 5′-CACGGUAUCUGGUCAUAAATT-3′; antisense strand: 5′-UUUAUGACCAGAUACCGUGGT-3′ was from Qiagen Sciences Inc. (USA). Trastuzumab (Herceptin) was purchased from Roche (USA). ProLong Gold antifade reagent with diamidino-2-phenylindole (DAPI) was purchased from Invitrogen (USA). DOXO HCl, FBS, Dulbecco's modified Eagle medium (DMEM), L-glutamine, penicillin/streptomycin, sodium pyruvate, minimum essential medium (MEM), and non-essential amino acids were purchased from Fisher Scientific (USA). Dialysis membrane tubing (molecular weight cutoff ≈ 3500 Da) was purchased from Spectrum Laboratories (USA). Herceptin PK Elisa kit was from MyBioSource (USA). Qubit microRNA assay kit was obtained from Life Technologies (Invitrogen, USA). The primary antibodies used for immunoblot analysis were anti-HER3 (1:1000; DAKO, USA), anti-HER2 (1:1000; CalbioChem, USA), anti-μ-tubulin (1:5000; Sigma-Aldrich, USA) from mouse, and anti-p-AKT (1:1000; Santa Cruz Biotechnology, USA) from rabbit. Cleaved caspase-3 immunostaining (#9661) was from Cell Signaling Technology (USA). Hematoxylin/eosin alcoholic (BioOptica). All other chemicals and solvents were of reagent grade (purchased from Sigma-Aldrich, USA). Sterile and nuclease free water was used for all aqueous solutions. All the chemicals were of analytical grade and used without further purification.

Synthesis of the PLGA Matrix: PLGA-core@Au-shell nanoconstructs (BGNs) were synthesized following a previously reported seeded-growth protocol with modifications.[79] For encapsulation in its polymeric PLGA core, DOXO was previously converted to its hydrophobic base as previously reported.[80] Briefly, DOXO base was obtained by means of an aqueous precipitation of DOXO·HCl aqueous solution (1 mg mL^{-1}) by adding triethylamine (three moles per drug mol) and methylene chloride. The system was kept under vigorous stirring for 1 h and then, the organic phase was removed and evaporated to recover DOXO base. Hereinafter, DOXO referred to DOXO base. To make the polymeric PLGA cores, 0.5 g of Pluronic F127 was dissolved in 50 mL of water and left overnight at room temperature to ensure homogenization. Next, a solution of 25 mg of PLGA (38–54 kDa) in 5 mL of acetone was made. This PLGA solution was mixed with 300 μg of DOXO, when corresponding, by sonication with a probe type sonicator (20 kHz, Bandelin Sonopuls, Bandelin GmbH, Germany) at 20 W for 10 min in an ice bath. Then, this organic solution was added dropwise with a syringe pump (0.166 mL min^{-1}) to the aqueous solution containing Pluronic F127 at a temperature below 10 °C under moderate stirring (250 rpm). The formed emulsion was homogenized with a sonicator tip at 100 W in an ice bath for 10 min. Then, acetone was left evaporated overnight under mechanical stirring. Nonencapsulated DOXO and the excess of F127 were eliminated by centrifugation twice at 9000 rpm for 40 min at 20 °C. Subsequently, the obtained supernatant was removed, and the precipitate was resuspended in 5 mL of water. The final PLGA NP suspension was filtered with a 0.45 μm filter (Millipore, USA). The obtained PLGA NPs had a hydrodynamic diameter and ζ-potential of 90 ± 20 nm and −39 ± 8 mV, respectively. The concentration of encapsulated DOXO inside the polymeric particles was determined by measuring the DOXO concentration in the supernatant by UV–vis spectroscopy using a previously obtained drug calibration curve and subtracting this value to the initial fed drug concentration. The loaded drug was estimated to be, for example, 5.5 μM at 1×10^{11} NP mL^{-1}.

Synthesis of Citrate-Capped Au Nanoseeds: Citrate-capped gold seeds were prepared following the method previously reported by Jana et al.[81] Briefly, 10 mL of 2.56×10^{-4} M trisodium citrate was mixed with 0.125 mL of 0.010 M $HAuCl_3 \cdot H_2O$. Next, 0.30 mL of a 0.1 M ice cold $NaBH_4$ solution was added all at once to the former solution and mixed. The resulting solution turned orange pink immediately indicating NP formation. The measured average NP size from TEM was 4 ± 2 nm.

Preparation of BGNs: In order to grow the gold nanolayer around the PLGA cores, 25 mL of PLGA NPs were incubated for 4 h with 1.25 mL of chitosan (1% w/v in acetic acid). Chitosan, a biocompatible polycation, was adsorbed on the negatively charged surfaces of PLGA NPs by electrostatic attraction, reversing the NP surface charge to +4 mV. Excess of chitosan was eliminated by centrifugation twice at 9000 rpm for 15 min and 20 °C. Next, 1 mL of citrated stabilized Au seeds was deposited per 5 mL of chitosan-modified DOXO-loaded PLGA NPs for 6 h at 450 rpm. Nonattached gold seeds were eliminated by centrifugation once at 15 000 rpm for 15 min at 20 °C. Subsequently, a Au growth solution was prepared by dissolving 0.1 g of potassium carbonate in 196 mL of deionized water and subsequent addition of 4 mL of 0.025 M $HAuCl_4 \cdot H_2O$. This solution was aged 24 h prior to use, with a final pH between 9.5 and 10. The growth of the Au shell was achieved by mixing 1 mL of PLGA NP–seed precursor solution with 20 mL of the Au growth solution while stirring at 250 rpm

for 1 min. Then, a subsequent reduction step by addition of 250 µL of 0.5 M ascorbic acid to the former solution was made. BGNs were immediately formed, as noted by the blue coloration of the obtained solution. BGNs were left to stand overnight and washed twice by centrifugation at 3500 rpm for 20 min and 20 °C.

Synthesis of the HSA–ICG Complex: First, a solution of 5 µM HSA in MES buffer (pH 6.0; 50 mM) was made and heated at 60 °C for 15 min to partially break up the intramolecular disulfide bonds and expose free sulfhydryl groups to be available for future conjugations. ICG was noncovalently conjugated to HSA by mixing both reactants under ambient conditions: 10 mL of 5 µM HSA and 10 mL of 30 µM ICG both in 50 mM 2-(N-morpholino)ethanesulfonic acid (MES) buffer at pH 6.0 were mixed and shaken for 4 h at room temperature. Then, to remove unbound ICG, the solution mixture was dialyzed for 24 h against MES buffer with a cellulose dialysis membrane with molecular weight cutoff (MWCO) of 3500 Da. Absorbance peaks of the protein–dye complex ($\lambda_{max} = 780$ nm) and bare protein ($\lambda_{max} = 280$ nm) were monitored to account for free-dye removal. It was estimated that 5 ICG molecules were bound per HSA protein one. The HSA–ICG complex was stored at 4 °C and protected from light before use.

Trastuzumab and siRNA Conjugation: To attach the antibody TZ and the siRNA to BGNs, the following steps were performed. First, HSA–ICG complex was filtered with a 0.22 µm filter (Millipore, USA). 2 mL of HSA–ICG complex (5×10^{-6} mol of HSA) was mixed with 3 mg of EDC and 3 mg of sulfo-NHS for 20 min in the dark. In this way, EDC reacted with the HSA carboxyl groups forming an amine-reactive *O*-acylisourea intermediate that quickly reacted with an amino group of sulfo-NHS to form a stable amide bond. Second, the activated HSA–ICG–NHS complex was conjugated with TZ upon mixing with 20 µg of the antibody. This solution was left in the dark for 2 h using an Incubator Minishaker (VWR, USA) at 300 rpm. Next, in a typical procedure, 2 mL of BGNs ($\approx 1.0 \times 10^{11}$ NPs mL^{-1}) with an optical density (OD) at ≈1.0 at 800 nm was mixed with 2 mL of the HSA–ICG–TZ complex for 12 h in the dark. Afterward, BGNs–HSA–ICG–TZ nanoconjugates (BGNs@HSA–ICG–TZ) were centrifuged twice for 15 min at 3500 rpm and 20 °C in order to eliminate nonadsorbed complexes and resuspended in PBS. Finally, the desired amount of siRNA (dissolved in RNAse free water, typically 10 pmol for 5×10^9 NPs) was mixed with 2 mL of BGNs@HSA–ICG–TZ particles at 37 °C for 4 h in a VWR Incubator Minishaker at 300 rpm. This siRNA possessed enough thiol groups that could establish disulfide bridges with free thiols of HSA and/or thiol—Au bonds from the metal BGN surface. The final platform was centrifuged once for 10 min at 3500 rpm and 20 °C. To quantify the amount of TZ loaded in the nanoplatform, an Elisa Kit assay was performed, while the fluorescent Qubit microRNA kit was employed to determine the siRNA loaded amount, following manufacturer's instructions.

Nanoplatform Characterization: NP sizes were obtained by dynamic light scattering (DLS) at 25 °C by means of an ALV-5000F (ALV-GmbH, Germany) instrument with vertically polarized incident light ($\lambda = 488$ nm) supplied by a diode-pumped neodymium-doped yttrium-aluminium-garne (Nd:YAG) solid-state laser (Coherent Inc., CA, USA) operated at 2 W, and combined with an ALV SP-86 digital correlator (sampling time 25 ns to 100 ms). NP sizes and morphologies were also acquired by TEM by means of a Phillips CM-12 and a Carl Zeiss Libra 200 FM Omega electronic microscopes operating at 120 kV. ζ-potentials were measured with a Zetasizer Nano ZS (Malvern, UK) using disposable folded capillary cells. Samples were measured at least in triplicate in PBS (pH 7.4) at 25 °C. The gold concentration in solution was determined by inductively coupling plasma mass spectrometry in a Varian 820-MS equipment (Agilent Technologies, USA). The corresponding concentration of BGNs@HSA–ICG–TZ/siRNA and DOXO-loaded BGNs@HSA–ICG–TZ/siRNA NPs was calculated by assuming a sphere model. UV–vis spectra were measured in a Cary Bio 100 UV–vis spectrophotometer (Agilent Technologies, USA). Fluorescence spectra were monitored in a Cary Eclipse spectrophotometer (Agilent Technologies, USA).

Colloidal Stability: A dilution of 1:50 for BGNs@HSA–ICG–TZ/siRNA NPs in PBS at pH 7.4, or sodium citrate–citric acid buffer of pH 5.5 supplemented with 10% v/v of FBS was carried out to perform the stability assay. Samples were placed in a temperature-controlled bath at 37 °C and stirring speed of 100 rpm. 1 mL of each sample was collected at regular time intervals and the NP's size was measured by DLS at 37 °C. Then, the samples were returned. Experiment was performed along an extended incubation (40 days).

Laser Irradiation Experiments: Temperature increment tests were performed using a continuous-wave-fiber-coupled diode laser source of 808 nm wavelength (50 W, Oclaro Inc., USA). The laser was powered by a Newport 5700-80-regulated laser diode driver (Newport Corporation, USA). A 5 m long, 200 µm core optical fiber was used to transfer the laser power from the laser unit to the target solution, and was equipped with a lens telescope mounting accessory at the output which allowed the tuning of the laser spot size in the range 1–10 mm. The output power was independently calibrated using an optical power meter (Newport 1916-C), and the laser spot size was previously measured with a laser beam profiler (Newport LBP-1-USB) placed at the same distance from the lens telescope output as the NP sample holder (8 cm). For measuring the temperature change mediated by the present hybrid NPs, 2 mL of hybrid BGNs@HSA–ICG NPs (OD ≈ 1.0) was irradiated at different power intensities. The sample temperature was measured with a type J thermocouple linked to a digital thermometer inserted into the solution. Pure buffer solution was used as a control.

In Vitro Release Studies: ICG, DOXO, TZ, and siRNA cumulative release profiles from BGNs were measured in vitro at a constant temperature of 37 °C under 300 rpm magnetic stirring for several days at pH 7.4, and at pH 5.5. To obtain the release profiles, 1 mL of BGNs was placed into dialysis tubes (SpectraPore, MWCO 3.5 kDa) located into 50 mL buffer supplemented with 10% v/v FBS at the pH of interest. The cumulative release was obtained by withdrawing 1 mL of the buffer medium at each sampling time, replacing it with the same volume of fresh buffer to maintain the required sink conditions. The DOXO and ICG contents in the buffer solution were obtained by means of UV–vis and fluorescence measurements, employing the calibration curves previously obtained in the corresponding buffers. UV–vis spectra were measured in a Cary Bio 100 UV–vis spectrophotometer (Agilent Technologies). The fluorescence of DOXO ($\lambda_{exc} = 485$ nm; $\lambda_{em} = 580$ nm) and ICG ($\lambda_{exc} = 789$ nm; $\lambda_{em} = 814$ nm) were measured in a FLUOstar OPTIMA microplate reader (BMG LABTECH, Germany). siRNA was quantified using the Qubit microRNA assay kit and TZ through ELISA, as mentioned previously. Experiments were carried out in triplicate. On the other hand, to decipher the effect of laser exposure in the DOXO, TZ, and siRNA release profiles, 1 mL of BGNs (1.0×10^{11} NP mL^{-1}) was incubated at 37 °C under moderate stirring at pH 5.5. The procedure was similar as described above with the only difference that after 6 and 24 h, samples were exposed at NIR 808 nm continuous-wave (CW) diode laser light (0.5 and 2.0 W cm^{-2}, respectively) for 3 min each.

Tumoral Cells: SKBR-3 breast cells from ATCC (Manassas, VA, USA) were used. Cells were grown at standard culture conditions (5% CO_2 at 37 °C) in McCoy's 5a medium modified supplemented with 10% v/v FBS.

In Vitro Cell Cytotoxicity: Cytotoxicity of the developed nanoplatforms was tested in vitro by the cell counting kit-8 (CCK-8) cytotoxicity assay in the presence and absence of NIR light irradiation. Breast SKBR-3 cancer cells with an optical confluence of 80–90% were seeded into 96-well plates (1.5×10^4 cells per well) and grown for 24 h at standard culture conditions in 100 µL growth medium. After 24 h of incubation at 37 °C and 5% CO_2, the corresponding tested nanoplatforms were added, suspended in 100 µL of growth medium to the wells. Wells without particles were left as a negative control (blank). In the absence of light illumination and after 24 or 48 h of further incubation, 10 µL of CCK-8 reagent was added to each well, and after 2 h, the absorption at 450 nm was measured with an UV–vis microplate absorbance reader. A similar procedure was followed for irradiated samples, but in this case, after 6 h of nanoparticle incubation, the culture medium was discarded, cells were washed with 10 mM PBS, pH 7.4, several times, and new culture medium (100 µL) was added. A set of cells was illuminated with the 808 nm CW diode laser at power fluencies of 0.5 and 2.0 W cm^{-2} for 5 min. Next, cells were left incubated for additional 18 or 42 h. Cell viability was calculated as survival rate = (Abs_sample/Abs_blank) ×100; where Abs_sample is the absorbance at 450 nm from samples and Abs_blank is the absorbance from blank controls (without nanoplatforms).

Western Blotting: SKBR-3 cells were incubated with the different nanoplatform configurations (BGNs@HSA–ICG, BGNs@HSA–ICG/siRNAsc, BGNs@HSA–ICG–TZ/siRNAsc, and BGNs@HSA–ICG–TZ/siRNA NPs) at a fixed concentration of 5.0×10^9 NP mL^{-1} for 24 and 48 h. For irradiated samples, same protocol as cell toxicity was followed. Western blot analysis was performed for HER3, HER2, p-AKT, and tubulin (as a loading control) protein expression. A typical procedure was followed, that consisted of washing twice the plates with ice-colded PBS before adding ice-colded lysis buffer (0.14 M NaCl, 0.05 M ethylenediaminetetraacetic acid, 1% glycerol, 0.1% IGEPAL 0.02 M Tris pH 7, 30 µL mL^{-1} aprotinin, 10 µL mL^{-1} phenylmethylsulfonyl fluoride, 10 µL mL^{-1} sodium orthovanadate, 50 mM NaF). After centrifugation (10 000 rpm, 10 min, 4 °C) to separate cellular debris, the lysates were resolved using denaturing gel electrophoresis (in an 8% polyacrylamide gel), and electrotransferred onto a nitrocellulose membrane (Schleicher and Schuell, Dassel, Germany).

In Vivo Biodistribution: NMRI-Fox1nu/Fox1nu nude mice (6 weeks old) were purchased from an authorized provider (Janvier Labs). All mice were housed in a microisolator cage system under specific pathogen-free conditions at room temperature with a 12 h light/dark cycle and fed with pellets and water ad libitum. The Experimental Animal Committee of USC approved the animal study (protocol no. 150005AE/13/FUN01/FIS02/JACP2); consequently, all animal experiments met the Animal Welfare guidelines. To assess the in vivo performance of the developed hybrid NPs, 8.0×10^6 cells from SKBR-3 adenocarcinoma breast cell line were injected subcutaneously in the dorsal flank of mice. At day 24 after the cell injection, 10 mg kg^{-1} of BGNs@HSA–ICG–TZ NPs was injected via the tail vein. The in vivo fluorescent activity ($\lambda_{ex}/\lambda_{em}$ = 710/ 840 nm) was registered with an IVIS Spectrum imaging system (Perkin-Elmer Inc., USA) at 24 and 48 h after NP administration. Mice were anesthetized using isoflurane during image acquisition. After 96 h upon injection, mice were euthanized and their organs harvested for subsequent analysis. Samples for TEM were fixed in 2% v/v glutaraldehyde in 0.2 M *N*-(2-hydroxyethyl)piperazine-29-(2-ethane-sulfonic acid) pH 7.4 overnight, washed again in cacodylate buffer 0.1 M pH 7.4, and postfixed with 2% v/v osmium tetroxide in cacodylate buffer at room temperature for 1 h. Organs were then embedded in agar, dehydrated with ethanol, and finally embedded in EPON resin. Staining with uranyl acetate was omitted to avoid potential false positives.

In Vivo Therapeutic Activity and Histology: Mice were housed in specific pathogen-free conditions, following Federation of European Laboratory Animal Science Associations guidelines for animal housing. The care and use of all experimental animals was in accordance with institutional guidelines and approved by the Ethics Committee of the University of Santiago de Compostela and Xunta de Galicia (approval ID 150005AE/13/FUN01/FIS02/JACP2). To assess the in vivo performance of the developed hybrid NPs, 8.0×10^6 cells from SKBR-3 adenocarcinoma breast cell line were injected subcutaneously in the dorsal flank of NMRI-Fox1nu/Fox1nu nude mice (6 weeks old). A caliper was used to know the width and length of the tumors and then the formula: $\pi/6 \times$ length $\times$ width $\times$ height (0.5 mm was estimated for the height) was applied to know the tumor volume. At day 24 after the cell injection, 10 mg kg^{-1} of DOXO-loaded BGNs@HSA–ICG–TZ/siRNA NPs were injected intratumorally. After 6 and 24 h, laser irradiations were carried out in the corresponding animals, using a continuous-wave-fiber-coupled diode laser source of 808 nm wavelength (50 W, Oclaro Inc., USA). Before NP injection, mice were randomly divided into four groups (n = 6 per group): nontreatment without NPs, nonirradiated NPs (0.0 W cm^{-2}), low-power density light irradiation (0.5 W cm^{-2}), and high-power density light irradiation (2.0 W cm^{-2}). Subcutaneous and intratumorally injections of PBS were used as controls. The in vivo fluorescent activity ($\lambda_{ex}/\lambda_{em}$ = 710/840 nm) registered with an IVIS Spectrum imaging system (Perkin-Elmer Inc., USA). Mice were anesthetized using isoflurane during image acquisition. At the end of the experiment, mice were euthanized and their organs harvested for subsequent analysis. Samples were fixed in 10% formalin v/v overnight, subsequently dehydrated in 70% v/v ethanol, and embedded in paraffin wax. Histological analysis was assessed on sections stained with H&E. For immunohistochemical analysis, anticleaved caspase 3 (monoclonal), and phosphohistone H3 (polyclonal) were used as primary antibodies (Cell Signaling Inc., USA). Immunohistochemical analysis was performed using a universal second antibody kit that used a peroxidase-conjugated labeled dextran polymer (Envision Plus, Denmark).

Statistical Analysis: OriginPro (Version 2022, OriginLab Corporation, Northampton, MA, USA) was used for statistical analysis and graphing. Quantitative data were expressed as mean ± standard deviation (SD) of three independent experiments (n = 3), except for in vivo (n = 6). All the statistical analysis was assessed using a two-tailed Student's t-test. A p-value of less than 0.05 was considered statistically significant.

Supporting Information

Supporting Information is available from the Wiley Online Library or from the author.

Acknowledgements

E.V.-A. and I.G.-C. contributed equally to this work. This work was supported by the Agencia Estatal de Investigación (AEI) through Project No. PID2019-109517RB-I00) and from the Xunta de Galicia, Project No. ED431C2022/18. European Regional Development Funds are also acknowledged. A.A.-M. and P.T. also thank the International Scientific Partnership Program ISSP at King Saud University for additional funding of this research through Grant No. ISPP-144. This work also received financial support from the ISCIII, Ministerio de Economía y Competitividad (Grant No. PI15/01129; J.A.C.), and the AEI (Grant No. PID2020-113501RB-I00; J.A.C.). I.-G.C. thanks for financial support through Grant No. PRE/2011/131, and the Centro Singular de Investigación de Galicia accreditation Grant No. 2016–2019 ED431G/05).

Conflict of Interest

The authors declare no conflict of interest.

Data Availability Statement

The data that support the findings of this study are available from the corresponding author upon reasonable request.

Keywords

active targeting, branched gold nanoshells, HER2-overexpressing breast cancer, multidrug resistance, theranostic nanoplatforms

Received: May 10, 2023
Revised: July 6, 2023
Published online:

[1] C. Fonti, A. Saumet, A. Abi-Khalil, B. Orsetti, E. Cleroux, A. Bender, M. Dumas, E. Schmitt, J. Colinge, W. Jacot, M. Weber, C. Sardet, S. du Manoir, C. Theillet, *Int. J. Cancer* **2019**, *145*, 1299.
[2] C. Arienti, S. Pignatta, A. Tesei, *Front. Oncol.* **2019**, *9*, 1308.
[3] Y. Yarden, M. X. Sliwkowski, *Nat. Rev. Mol. Cell Biol.* **2001**, *2*, 127.
[4] X. Liu, S. Liu, H. Lyu, A. I. Riker, Y. Zhang, B. Liu, *Biol. Proced. Online* **2019**, *21*, 5.
[5] J. S. Ross, J. A. Fletcher, *Stem Cells* **1998**, *16*, 413.
[6] C. Knuefermann, Y. Lu, B. Liu, W. Jin, K. Liang, L. Wu, M. Schmidt, G. B. Mills, J. Mendelsohn, Z. Fan, *Oncogene* **2003**, *22*, 3205.

[7] K. Liang, W. Jin, C. Knuefermann, M. Schmidt, G. B. Mills, K. K. Ang, L. Milas, Z. Fan, *Mol. Cancer Ther.* **2003**, *2*, 353.
[8] W. Jin, L. Wu, K. Liang, B. Liu, Y. Lu, Z. Fan, *Br. J. Cancer* **2003**, *89*, 185.
[9] D. J. Slamon, G. M. Clark, S. G. Wong, W. J. Levin, A. Ullrich, W. L. McGuire, *Science* **1987**, *235*, 177.
[10] D. J. Slamon, B. Leyland-Jones, S. Shak, H. Fuchs, V. Paton, A. Bajamonde, T. Fleming, W. Eiermann, J. Wolter, M. Pegram, J. Baselga, L. Norton, *N. Engl. J. Med.* **2001**, *344*, 783.
[11] C. A. Hudis, *N. Engl. J. Med.* **2007**, *357*, 39.
[12] K. L. Jones, A. U. Buzdar, *Lancet Oncol.* **2009**, *10*, 1179.
[13] Z. Zhou, Y. Liu, W. Song, X. Jiang, Z. Deng, W. Xiong, J. Shen, *J. Controlled Release* **2022**, *352*, 793.
[14] Y. Liu, Z. Zhou, J. Hou, W. Xiong, H. Kim, J. Chen, C. Zheng, X. Jiang, J. Yoon, J. Shen, *Adv. Mater.* **2022**, *34*, 2206121.
[15] Z. Zhou, Y. Liu, X. Jiang, C. Zheng, W. Luo, X. Xiang, X. Qi, J. Shen, *Int. J. Biol. Macromol.* **2023**, *224*, 797.
[16] S. Wang, Z. Zhou, R. Hu, M. Dong, X. Zhou, S. Ren, Y. Zhang, C. Chen, R. Huang, M. Zhu, W. Xie, L. Han, J. Shen, C. Xie, *Adv. Sci.* **2023**, *10*, 2207608.
[17] T. Triulzi, L. Forte, V. Regondi, M. Di Modica, C. Ghirelli, M. L. Carcangiu, L. Sfondrini, A. Balsari, E. Tagliabue, *Oncoimmunology* **2019**, *8*, e1512942.
[18] S. Duro-Sánchez, M. R. Alonso, J. Arribas, *Cancers* **2023**, *15*, 1069.
[19] E. H. van der Horst, M. Murgia, M. Treder, A. Ullrich, *Int. J. Cancer* **2005**, *115*, 519.
[20] C. A. Ritter, M. Perez-Torres, C. Rinehart, M. Guix, T. Dugger, J. A. Engelman, C. L. Arteaga, *Clin. Cancer Res.* **2007**, *13*, 4909.
[21] D. Lee, M. Yu, E. Lee, H. Kim, Y. Yang, K. Kim, C. Pannicia, J. M. Kurie, D. W. Threadgill, *J. Clin. Invest.* **2009**, *119*, 2702.
[22] C. Desbois-Mouthon, *Gastroenterol. Clin. Biol.* **2010**, *34*, 255.
[23] E. Buck, A. Eyzaguirre, J. D. Haley, N. W. Gibson, P. Cagnoni, K. K. Iwata, *Mol. Cancer Ther.* **2006**, *5*, 2051.
[24] K. Kunii, L. Davis, J. Gorenstein, H. Hatch, M. Yashiro, A. Di Bacco, C. Elbi, B. Lutterbach, *Cancer Res.* **2008**, *68*, 2340.
[25] M.-S. Tsai, L. A. Shamon-Taylor, I. Mehmi, C. K. Tang, R. Lupu, *Oncogene* **2003**, *22*, 761.
[26] S. T. Lee-Hoeflich, L. Crocker, E. Yao, T. Pham, X. Munroe, K. P. Hoeflich, M. X. Sliwkowski, H. M. Stern, *Cancer Res.* **2008**, *68*, 5878.
[27] X. Li, Y. Lu, K. Liang, B. Liu, Z. Fan, *Breast Cancer Res.* **2005**, *7*, R589.
[28] J. T. Garrett, C. R. Sutton, R. Kurupi, C. U. Bialucha, S. A. Ettenberg, S. D. Collins, Q. Sheng, J. Wallweber, L. DeFazio-Eli, C. L. Arteaga, *Cancer Res.* **2013**, *73*, 6013.
[29] S. Paik, C. Kim, N. Wolmark, *N. Engl. J. Med.* **2008**, *358*, 1409.
[30] H.-H. Yuan, Y.-N. Yang, J.-H. Zhou, Y.-J. Li, L.-Y. Wang, J.-W. Qin, T. Liu, Z.-Z. Li, Q.-X. Zhou, X.-L. Wei, T.-T. Zhang, P. Huang, W.-J. Zhang, L. Liu, X.-X. Du, Y. Han, *OncoTargets Ther.* **2017**, *8*, 52584.
[31] X. Yu, S. Ghamande, H. Liu, L. Xue, S. Zhao, W. Tan, L. Zhao, S.-C. Tang, D. Wu, H. Korkaya, N. J. Maihle, H. Y. Liu, *Mol. Ther.–Nucleic Acids* **2018**, *10*, 317.
[32] A. Derakhshani, Z. Rezaei, H. Safarpour, M. Sabri, A. Mir, M. A. Sanati, F. Vahidian, A. Gholamiyan Moghadam, A. Aghadoukht, K. Hajiasgharzadeh, B. Baradaran, *J. Cell. Physiol.* **2020**, *235*, 3142.
[33] S. Bai, Y. Lan, S. Fu, H. Cheng, Z. Lu, G. Liu, *Nano-Micro Lett.* **2022**, *14*, 145.
[34] L. Racca, V. Cauda, *Nano-Micro Lett.* **2021**, *13*, 11.
[35] A. Topete, D. Melgar, M. Alatorre-Meda, P. Iglesias, B. Argibay, S. Vidawati, S. Barbosa, J. A. Costoya, P. Taboada, V. Mosquera, *J. Mater. Chem. B* **2014**, *2*, 6967.
[36] K. Bolaños, M. J. Kogan, E. Araya, *Int. J. Nanomed.* **2019**, *14*, 6387.
[37] S. Nakata, N. Kido, M. Hayashi, M. Hara, H. Sasabe, T. Sugawara, T. Matsuda, *Biophys. Chem.* **1996**, *62*, 63.
[38] S. Barbosa, A. Topete, M. Alatorre-Meda, E. M. Villar-Alvarez, A. Pardo, C. Alvarez-Lorenzo, A. Concheiro, P. Taboada, V. Mosquera, *J. Phys. Chem. C* **2014**, *118*, 26313.
[39] M. R. K. Ali, Y. Wu, M. A. El-Sayed, *J. Phys. Chem. C* **2019**, *123*, 15375.
[40] N. S. Abadeer, C. J. Murphy, *J. Phys. Chem. C* **2016**, *120*, 4691.
[41] W. Yang, H. Liang, S. Ma, D. Wang, J. Huang, *Sustainable Mater. Technol.* **2019**, *22*, e00109.
[42] R. Bardhan, N. K. Grady, J. R. Cole, A. Joshi, N. J. Halas, *ACS Nano* **2009**, *3*, 744.
[43] H. Wang, K. Fu, R. A. Drezek, N. J. Halas, *Appl. Phys. B: Lasers Opt.* **2006**, *84*, 191.
[44] R. Alvarez-Puebla, L. M. Liz-Marzán, F. J. García de Abajo, *J. Phys. Chem. Lett.* **2010**, *1*, 2428.
[45] I. B. Becerril-Castro, I. Calderon, N. Pazos-Perez, L. Guerrini, F. Schulz, N. Feliu, I. Chakraborty, V. Giannini, W. J. Parak, R. A. Alvarez-Puebla, *Analysis Sensing* **2022**, *2*, e202200005.
[46] N. V. Sergina, M. Rausch, D. Wang, J. Blair, B. Hann, K. M. Shokat, M. M. Moasser, *Nature* **2007**, *445*, 437.
[47] R. Xu, J. Sui, M. Zhao, Y. Yang, L. Tong, Y. Liu, Y. Sun, Y. Fan, J. Liang, X. Zhang, *Polym. Test.* **2022**, *113*, 107669.
[48] D. Gajria, S. Chandarlapaty, *Expert Rev. Anticancer Ther.* **2011**, *11*, 263.
[49] A. Topete, M. Alatorre-Meda, E. M. Villar-Alvarez, S. Carregal-Romero, S. Barbosa, W. J. Parak, P. Taboada, V. Mosquera, *Adv. Healthcare Mater.* **2014**, *3*, 1309.
[50] A. Topete, M. Alatorre-Meda, P. Iglesias, E. M. Villar-Alvarez, S. Barbosa, J. A. Costoya, P. Taboada, V. Mosquera, *ACS Nano* **2014**, *8*, 2725.
[51] H. J. Jang, M. G. Song, C. R. Park, H. Youn, Y. S. Lee, G. J. Cheon, K. W. Kang, *Int. J. Mol. Sci.* **2023**, *24*, 850.
[52] Z.-Y. Dai, C. Shen, X.-Q. Mi, Q. Pu, *Front. Surg.* **2023**, *10*, 1077492.
[53] R. Bardhan, W. Chen, M. Bartels, C. Perez-Torres, M. F. Botero, R. W. McAninch, A. Contreras, R. Schiff, R. G. Pautler, N. J. Halas, A. Joshi, *Nano Lett.* **2010**, *10*, 4920.
[54] Y. Wang, Y.-Y. Huang, Y. Wang, P. Lyu, M. R. Hamblin, *Sci. Rep.* **2017**, *7*, 7781.
[55] L. Zhang, Y. Zhang, D. Xing, *J. Cell. Physiol.* **2010**, *224*, 218.
[56] N. Bhatt, P.-J. J. Huang, N. Dave, J. Liu, *Langmuir* **2011**, *27*, 6132.
[57] M. S. Strozyk, M. Chanana, I. Pastoriza-Santos, J. Pérez-Juste, L. M. Liz-Marzán, *Adv. Funct. Mater.* **2012**, *22*, 1436.
[58] R. A. Sperling, W. J. Parak, *Philos. Trans. R. Soc., A* **2010**, *368*, 1333.
[59] W. Wei, X. Zhang, S. Zhang, G. Wei, Z. Su, *Mater. Sci. Eng., C* **2019**, *104*, 109891.
[60] X. Li, J. F. Lovell, J. Yoon, X. Chen, *Nat. Rev. Clin. Oncol.* **2020**, *17*, 657.
[61] M. Dockal, D. C. Carter, F. Rüker, *J. Biol. Chem.* **2000**, *275*, 3042.
[62] N. Sitte, in *Aging at the Molecular Level*, Springer, Dordrecht **2003**, pp. 27–45.
[63] J. Reichenwallner, M.-T. Oehmichen, C. Schmelzer, T. Hauenschild, A. Kerth, D. Hinderberger, *Magnetochemistry* **2018**, *4*, 47.
[64] K. Urbanska, B. Romanowska-Dixon, Z. Matuszak, J. Oszajca, P. Nowak-Sliwinska, G. Stochel, *Acta Biochim. Pol.* **2002**, *49*, 387.
[65] W. F. Zandberg, A. B. S. Bakhtiari, Z. Erno, D. Hsiao, B. D. Gates, T. Claydon, N. R. Branda, *Nanomedicine* **2012**, *8*, 908.
[66] T. P. Gustafson, Q. Cao, S. T. Wang, M. Y. Berezin, *Chem. Commun.* **2013**, *49*, 680.
[67] M. Borzenkov, G. Chirico, L. D'Alfonso, L. Sironi, M. Collini, E. Cabrini, G. Dacarro, C. Milanese, P. Pallavicini, A. Taglietti, C. Bernhard, F. Denat, *Langmuir* **2015**, *31*, 8081.
[68] T. Kute, C. M. Lack, M. Willingham, B. Bishwokama, H. Williams, K. Barrett, T. Mitchell, J. P. Vaughn, *Cytometry* **2004**, *57A*, 86.
[69] D. N. Amin, M. R. Campbell, M. M. Moasser, *Semin. Cell Dev. Biol.* **2010**, *21*, 944.
[70] S. Wang, X. Huang, C.-K. Lee, B. Liu, *Oncogene* **2010**, *29*, 4225.
[71] M. Campiglio, G. Somenzi, C. Olgiati, G. Beretta, A. Balsari, N. Zaffaroni, P. Valagussa, S. Ménard, *Int. J. Cancer* **2003**, *105*, 568.
[72] M. R. Hamblin, *Photochem. Photobiol.* **2018**, *94*, 199.
[73] A. S. C. Foo, T. W. Soong, T. T. Yeo, K.-L. Lim, *Front. Aging Neurosci.* **2020**, *12*, 00089.

[74] J. B. Wolinsky, Y. L. Colson, M. W. Grinstaff, *J. Controlled Release* **2012**, *159*, 14.
[75] A. Huang, M. M. Pressnall, R. Lu, S. G. Huayamares, J. D. Griffin, C. Groer, B. J. DeKosky, M. L. Forrest, C. J. Berkland, *J. Controlled Release* **2020**, *326*, 203.
[76] H.-J. Jhan, J.-J. Liu, Y.-C. Chen, D.-Z. Liu, M.-T. Sheu, H.-O. Ho, *Nanomedicine* **2015**, *10*, 1263.
[77] B. Gao, J. Luo, Y. Liu, S. Su, S. Fu, X. Yang, B. Li, *Int. J. Nanomed.* **2021**, *16*, 4073.
[78] Y. Yao, Y. Zang, J. Qu, M. Tang, T. Zhang, *Int. J. Nanomed.* **2019**, *14*, 8787.
[79] J. Yang, J. Lee, J. Kang, S. J. Oh, H.-J. Ko, J.-H. Son, K. Lee, J.-S. Suh, Y.-M. Huh, S. Haam, *Adv. Mater.* **2009**, *21*, 4339.
[80] T. K. Jain, J. Richey, M. Strand, D. L. Leslie-Pelecky, C. A. Flask, V. Labhasetwar, *Biomaterials* **2008**, *29*, 4012.
[81] N. R. Jana, L. Gearheart, C. J. Murphy, *J. Phys. Chem. B* **2001**, *105*, 4065.